Generation of isolated white-light attosecond pulses in solids

Gefei Li,[1,2] Hao Teng,[1,2,3,*] Zhiyi Wei,[1,2,3,†] Sheng Meng,[1,2,3] and Pengju Zhang[1,2,3,‡]
[1]*Institute of Physics, Chinese Academy of Sciences, Beijing 100190, China*
[2]*School of Physical Sciences, University of Chinese Academy of Sciences, Beijing 100190, China*
[3]*Songshan Lake Materials Laboratory, Dongguan, Guangdong 523808, China*

(Received 28 March 2025; revised 15 September 2025; accepted 22 December 2025; published 22 January 2026)

Attosecond-pump attosecond-probe spectroscopy (APAP) is the key to understanding electronic-dominated dynamics in light-matter interactions. Although the feasibility of APAP has been demonstrated using isolated attosecond pulses (IAPs), the efforts are mainly confined to the ionization-induced dynamics triggered by the extreme ultraviolet and soft x-ray lights. However, the generation of IAPs capable of exciting neutral electronic excited states, which are more prevalent in nature, is still in its infancy, significantly limiting comprehensive insights into valence-electron wave packet dynamics. Here, we theoretically demonstrate a scheme for the straightforward and compact generation of white-light IAPs covering the visible and ultraviolet regions, based on solid-state high-harmonic generation. By analyzing the strong-field-induced electron-hole dynamics together with a saddle-point approximation, we unfold its microscopic generation mechanism. Furthermore, the feasibility and robustness of this approach are validated by the generation of IAPs from various materials under the same mechanism. Our work paves the way for generation of tabletop white-light IAP sources, thereby harnessing the widespread applications of APAP.

DOI: 10.1103/8x1z-3l7k

The advent of attosecond laser pulses via high-harmonic generation (HHG) [1,2] has undoubtedly revolutionized the field of light-matter interactions. Over the past three decades, the widespread use of attosecond pulses, particularly in studying electron dynamics in atoms [3–6], molecules [7–9], liquids [10,11], and solids [12–14], has led to the emergence of attosecond science [15,16]. However, the vast majority of attosecond science experiments are performed by combining attosecond pulses with intense femtosecond near-infrared (NIR) pulses. The temporal resolution of this extreme ultraviolet (XUV)-NIR pump-probe scheme is primarily limited by the cross-correlation between the two pulses, typically on the order of a few femtoseconds, preventing the study of valence electron motion on the attosecond to femtosecond timescale [17]. In principle, a true attosecond-pump attosecond-probe spectroscopic (APAP) protocol can overcome this bottleneck.

Yet, isolated attosecond pulses (IAPs) from gas-phase HHG sources [18–23] have extremely low photon flux due to poor conversion efficiency, limiting their applications as either pump or probe pulse. With a significant higher photon flux, x-ray free-electron lasers (XFELs) enable the APAP measurements well suited for core-electron dynamics [11], while their limited availability restricts widespread applications. For both gas- and solid-state HHG [24–27], extensive efforts are focused on extending the plateau region, which can, in principle, generate Fourier transform-limited attosecond pulses with wavelengths predominantly confined to the XUV region. Contrasting with the gas-phase HHG process, which is generally well described by a semiclassical model [28], solid-state HHG, pioneeringly achieved since 2010 [29], remains its principal microscopic mechanism in a formative stage [30,31].

In the solid-phase HHG, the attosecond chirp [32] can be optimized by a designed laser waveform thanks to the field-driven Bloch oscillations of the electron wave packet [33] (see detailed discussion in the Supplemental Material [34]). This offers a controllable parameter for balancing the plateau width and pulse duration. Leveraging the modifiable electron dynamics in solids, recent advances have optimized HHG spectra to region of tens of attoseconds, featuring a quasicontinuum plateau in the XUV region [24–27,35–37]. Despite these successes, the increasing attempts toward studying attosecond valence-electron dynamics [17] ultimately necessitate the generation of IAPs in the deep ultraviolet to visible spectral region.

In this article, supercontinuum chirp-free white-light IAPs are achieved by coherently manipulating electron wave packet dynamics in solid-state samples, enabled through crystal self-chirp compensation (CCC) scheme (see Fig. 1) with a simply waveform-tailored laser pulse. In addition to the adjustable pulse duration, our findings also reveal the remarkable flexibility in polarization manipulation of IAPs, enabling seamless switching between linear and circular polarization states. Facilitated by the physical insights from the semiclassical collision model and verified through quantum dynamical

*Contact author: hteng@iphy.ac.cn
†Contact author: zywei@iphy.ac.cn
‡Contact author: pengju.zhang@iphy.ac.cn

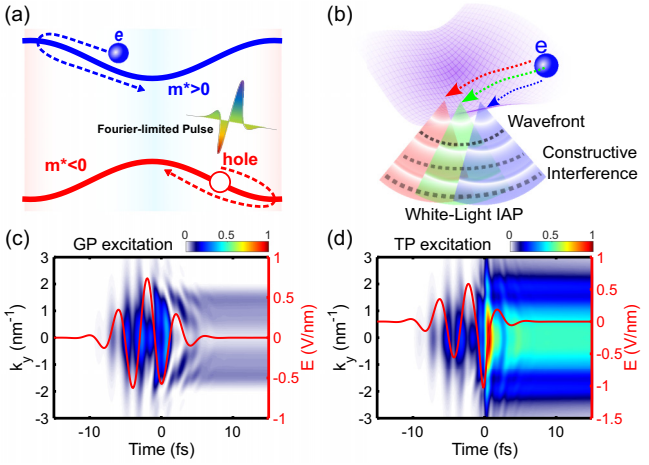

FIG. 1. (a) Principle of crystal self-chirp compensation: Under the driving of an ideal optical field, the phases accumulated by electrons moving in regions of positive effective mass (negative chirp) and negative effective mass (positive chirp) mutually compensate, resulting in the generation of transform-limited radiation upon electron-hole recombination. (b) Schematic of white-light IAP generation. Controlling wave packet dispersion enables constructive interference between quantum pathways (color-coded by photon energy), generating a supercontinuum. (c), (d) Evolution of $|\rho_{cv}|$ with time and crystal momentum under a Gaussian pulse (GP) and a tailored pulse (TP), respectively. The red lines represent the corresponding electric driven fields.

simulations, we elucidate the underlying microscopic mechanism and develop a straightforward model for evaluating suitable light waveforms and material systems.

Specifically for solid-state HHG, the presence of band dispersion naturally introduces group velocity delay into the light field-driven electron dynamics. Considering the correspondence between the dispersion of electron-hole wave packet and the chirp of the corresponding coherent radiation, the emitted HHG spectrum is intrinsically broadened by this imprinted dispersion from the field-driven electron-hole wave packet, deviating from the transform-limited condition. In analogy to achieving the shortest pulse duration through a dispersion-specific medium, the electron band structure naturally provides a platform to encode both negative and positive dispersion on the evolving electron-hole wave packet.

Figure 1 (a) clearly shows that the field-driven electron-hole wave packet can gain negative chirp ($d\omega/dk > 0$) in the region of positive effective mass, which lately can be compensated in the region of negative effective mass (positive chirp, $d\omega/dk < 0$) [38,39]. By manipulating the electron-hole wave packet's dispersion, constructive interference between different harmonic emission channel can be achieved through phase modulation between different quantum pathways, as illustrated in Fig. 1(b). According to symmetry analysis, the enhancement of odd harmonics and suppression of even harmonics originate from the system's inversion symmetry and the driving field's time-translation symmetry [40]. Therefore, breaking time-translation symmetry and engineering dynamical symmetry via the driving waveform is essential, which can be flexibly synthesized through optical approach. To showcase this point, we compare the electron dynamics driven by a designed optical waveform and a Gaussian pulse with comparable intensity and frequency, as shown in Figs. 1(c) and 1(d), respectively. Given that dispersion during HHG emission primarily arises from interband radiation, we first present the amplitude of the off-diagonal elements of the density matrix ρ_{cv}, illustrating the behavior of electron-hole wave packets in k space. The phase evolution over time and changes in conduction band population are discussed in later sections and provided in the Supplemental Material [41]. In waveform-tailored case, ρ_{cv} displays a well-localized transient burst that appears and vanishes rapidly, which indicates the possibility of radiation emission with an ultrashort duration.

Considering this unique dispersion framework of solid materials, we focus on investigating the electron-hole wave packet by tailoring the driving field $\mathbf{E}(t)$ according to the semiclassical Bloch acceleration theory $\dot{\mathbf{k}}(t) = -\frac{e}{\hbar}\mathbf{E}(t)$[42]. To examine this, we first analyze the phase composition of electron-hole wave packets.

Under the Keldysh adiabatic approximation $\rho_{vv} - \rho_{cc} \approx 1$ and the first-order $\mathbf{k}\cdot\mathbf{p}$ model $\mathcal{A}_{mn}(\mathbf{k}(t)) = d_0\varepsilon_g/\varepsilon_g(\mathbf{k}(\mathbf{t}))$, with $\varepsilon_g(\mathbf{k}) = \varepsilon_c(\mathbf{k}) - \varepsilon_v(\mathbf{k})$, ε_g the band gap, and $\mathcal{A}_{mn}$ the matrix element of transition dipole, the formal solution of the interband current can be written as [43]

$$\begin{aligned}\mathbf{J}_{\text{inter}}(t) = &-\frac{e^2}{\pi^2\hbar^2}\varepsilon_g^2 d_0^2 \int_{\text{BZ}} d\mathbf{k} \int_{-\infty}^{t} \frac{\mathbf{E}(t)}{\varepsilon_g(\mathbf{k}(t))} \\ &\times e^{-i\int_{t'}^{t} dt''[\varepsilon_g(\mathbf{k}(t''))/\hbar + e\mathbf{E}(t)\cdot\mathbf{A}(k(t''))/\hbar]} \\ &\times e^{-i(\arg[\mathbf{d}(\mathbf{k}))] - e/\hbar \arg[\mathbf{E}(t)\cdot\mathbf{d}(\mathbf{k}(\mathbf{t},\mathbf{t}'))])} e^{-(t-t')/T_2 dt'} \\ &+ \text{c.c.}, \end{aligned} \tag{1}$$

where BZ is the first Brillouin zone and $\mathcal{D}(t', t, \mathbf{k}) = \frac{1}{\hbar}\int_{t'}^{t} dt'' \varepsilon_g(\mathbf{k}(t''))$ is the dynamical phase and $\mathcal{B} = \arg[\mathbf{d}(\mathbf{k}))] - e/\hbar \arg[\mathbf{E}(t)\cdot\mathbf{d}(\mathbf{k}(\mathbf{t},\mathbf{t}'))] + \int_{t'}^{t} dt'' e\mathbf{E}(t)\cdot\mathbf{A}(k(t''))/\hbar$ is the topological phase [44]. Note that inclusion of the topological phase results in it being gauge invariant. Expanding the dynamical phase in the vicinity of band-gap minima $\mathbf{k_0}$, we have $\mathcal{D}(t', t, \mathbf{k}) = \frac{1}{\hbar}\int_{t'}^{t} dt'' \varepsilon_g + \frac{\partial\varepsilon}{\partial k}|_{k=k_0}(\mathbf{k}-\mathbf{k_0}) + \frac{1}{2}\frac{\partial^2\varepsilon}{\partial k^2}|_{k=k_0}(\mathbf{k}-\mathbf{k_0})^2 + o[(\mathbf{k}-\mathbf{k_0})^2)]$.

In the expression on the right-hand side, the second term represents the electron group velocity, v_g. The third term is the effective mass, $\frac{1}{m_b^*}$, which dominates the dynamics of the electron-hole wave packet. The same procedure can be applied to topological phase $\mathcal{B}$ as well. The anomalous velocity v_a arises from the Berry phase, determining another contribution to the wave packet spreading, whereas $\partial_k^2\mathcal{B}$ describes the wave packet chirp induced by this anomalous velocity ($\frac{1}{m_a^*}$). The phase of the interband dipole matrix element accounts for the contributions of band renormalization to wave packet dynamics. Herein, we define the group velocity $v_{c,n}^*$ and wave packet dispersion $\frac{1}{m_n^*}$ to label its contribution. For simplicity, we define $v_{c,v}^* = v_{c,v|g}^* + v_{c,v|a}^* + v_{c,v|n}^*$ and $\frac{1}{m_{c,v}^*} = \frac{1}{m_{c,v|b}^*} + \frac{1}{m_{c,v|a}^*} + \frac{1}{m_{c,v|n}^*}$. We find that Berry curvature plays a negligible role in the present system (see the Supplemental Material for details [45]), while it can significantly influence electron recollision dynamics in many prototypical topological materials [46]. To obtain a transform-limited pulse, the total phase ϕ_{total} must

satisfy the following conditions:

$$\left.\frac{\partial \phi_{\text{total}}}{\partial \mathbf{k}}\right|_{t=t_r} = \frac{1}{\hbar}\int_{t'}^{t} dt''[v_c^* - v_v^*]\Big|_{t=t_r} = 0,$$
$$\left.\frac{\partial^2 \phi_{\text{total}}}{\partial \mathbf{k}^2}\right|_{t=t_r} = \hbar\int_{t'}^{t} dt''\frac{1}{m_c^*} - \frac{1}{m_v^*}\Big|_{t=t_r} = 0. \quad (2)$$

The first equation indicates that the electron and hole recombine at $t = t_r$. Simultaneously, the dispersion of the electron-hole pair (wave packet) $1/m_{e-h}^* = 1/m_c^* - 1/m_v^*$ is fully compensated at $t = t_r$, which is reflected in the second equation.

To validate the feasibility of our model, the simulated annealing algorithm, characterized by its insensitivity to initial conditions and global optimization capability, is employed to perform waveform tailoring. Details of the simulated annealing algorithm [47,48] can be found in the Supplemental Material [49]. Considering the feasibility of experiment, we synthesize the driving waveform simply by superposing two arbitrary Gaussian envelopes.

The objective function is defined as $f = \int_{\text{BZ}} |\rho_{cv}|^2 |\frac{\partial(\mathcal{D}+\mathcal{B})}{\partial \mathbf{k}}|^2 |\frac{\partial^2(\mathcal{D}+\mathcal{B})}{\partial \mathbf{k}^2}|^2|_{t=t_r}$, where $|\rho_{cv}|^2$ serves as a weighting factor. The ρ_{cv} and harmonic currents are calculated using the Houston-based semiconductor Bloch equations [50] (see details in the Supplemental Material [51]). The key of dynamical control lies in breaking the discrete time-translation symmetry and enhancing constructive interference between different quantum paths. A tailored two-pulse Gaussian sequence enables selective pathway amplification while maintaining experimental feasibility for waveform synthesis. To benchmark our approach, we start with a gapped graphene model with a 2 eV band gap and a dephasing time of $T_2 = 10$ fs (see the Supplemental Material for details [52]). This system is irradiated by a standard Gaussian pulse with a central wavelength of 1.256 μm [red dashed line in Fig. 2(a)] to obtain the HHG spectrum. (This Gaussian pulse exhibits the closest electric field profile to that of our tailored pulse.) Figure 2(b) shows the simulated HHG spectra, exhibiting discrete harmonics at odd multiples of the fundamental photon energy. Importantly, these harmonic orders can be generated at any temporal instant of the GP pulse. Figure 2(d) presents the frequency-domain profile of a broadband pulse generated by the interaction between the tailored pulse (TP) [see the red dashed line in Fig. 2(c)] and gapped graphene. The photoenergy of this pulse varies from near 0 to 8 eV with its central energy around 3.5 eV, fully covering the white-light region. The temporal duration of this white-light pulse is obtained as 460 as by the time-frequency analysis, which is indicated as the purple region in Fig. 2(c). Around $t = 0$, the harmonic radiation spreads a continuous spectrum perpendicular to the time axis, exhibiting clear characteristics of a transform-limited pulse.

Following Refs. [53,54], we employ waveform engineering to simultaneously localize both the tunneling/emission timing and crystal momentum distribution of electron-hole pairs. By ensuring these pairs experience an isotropic environment during radiation, our approach enables generation of near-circularly polarized isolated attosecond pulses. The temporal and frequency spectra are shown in Figs. 2(e) and 2(f),

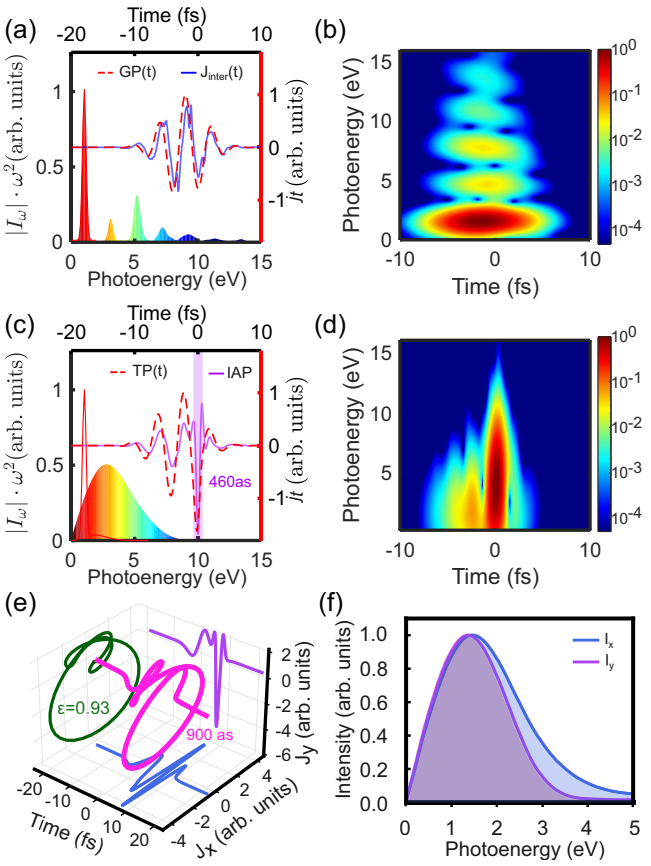

FIG. 2. (a) Nonlinear current (blue solid line) generated by the interaction of a GP with a central wavelength 1.256 μm (red dashed line) with gapped graphene. The colored area represents its spectra. (b) Time-frequency analysis spectrum of the time-domain current in panel (a). Panels (c) and (d) are similar to panels (a) and (b), respectively, but for TP excitation. (e) Frequency-domain spectra and ellipticity of the circularly polarized (CP) IAP. (f) Temporal field of CPIAP. The ellipticity here is defined as $\epsilon = \frac{E_x}{E_y}$. The parameters of the driving laser used in the figure are listed in the table in the Supplemental Material [57]. Gabor transform was performed by optfrog package [58].

respectively. It is found that the ellipticity of this transform-limited pulse is about 0.93 and its duration is estimated as 900 as, enabling the study of valley, spin, and chiral molecules in materials in attosecond timescale [55,56].

Having demonstrated the feasibility of waveform tailoring in generating both linearly and circularly polarized IAPs, we now unveil the underlying mechanism driving the emission of continuous spectrum. Within the framework of perturbative nonlinear optics, the coherent emissions are naturally explained as being strictly confined to integer multiples of the driving frequency. This result emerges when the interference between quantum transition pathways at different frequencies can be neglected [59]. Nevertheless, as the driving intensity increases to the nonperturbative regime, the interference between different quantum paths can no longer be neglected, therefore raising opportunities for manipulating excitation dynamics.

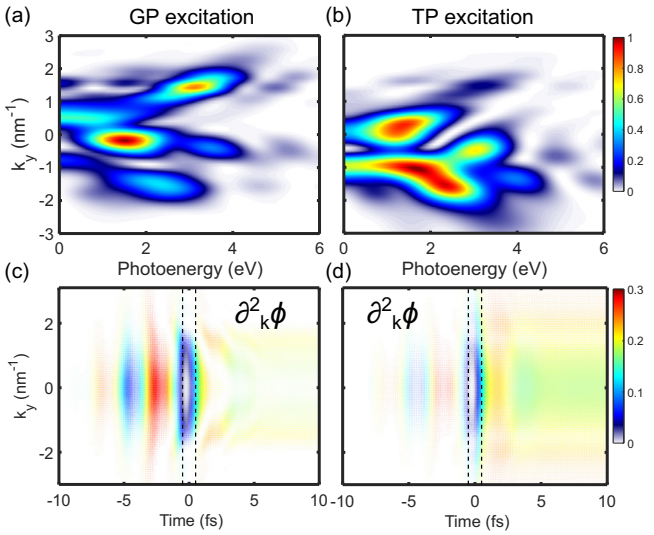

FIG. 3. Panels (a) and (b) show the HHG intensity distributions along the $k_x = 0\,\mathrm{nm}^{-1}$ axis under excitation by a GP and a TP pulse, respectively. Panels (c) and (d) display the corresponding $\partial_k^2\phi$ with respect to k along the same $k_x = 0\,\mathrm{nm}^{-1}$ axis. The transparency of each data point is weighted by the magnitude of ρ_{cv}. The dashed area indicates the region where the IAP is generated by the TP pulse.

To gain deeper insights into the microscopic mechanisms, we analyze the momentum-resolved electron-hole pair contributions to high-harmonic generation for both GP and TP pulse excitations in Figs. 3(a) and 3(b), respectively. Under GP excitation, (1) destructive interference between quantum paths of different harmonic orders occurs at the same k point and (2) destructive interference between quantum paths at different k points leads to the pronounced, discrete harmonic structure. In contrast, TP excitation is optimized such that the electron-hole wave packet dispersion vanishes at $t = t_r$, enforcing constructive interference among quantum paths originating from the same k point. Simultaneously, the minimization of weighted dispersion across the entire k space suppresses destructive interference between different k points. As a result, Fig. 3(b) reveals a relatively continuous harmonic-photon emission distribution along both the crystal momentum and photon energy axes.

To better illustrate this dynamics, we show the acquired field-driven dynamical and topological phases for the two pulse excitations in Figs. 3(c) and 3(d), respectively. At the harmonic emission time, the TP excitation drives $\partial_k^2\phi$ rapidly to zero before it swiftly increases again. In contrast, under Gaussian excitation $\partial_k\phi$ remains finite and nearly uniform throughout k space, consistent with the broad wave packet spreading of electron-hole pairs observed each half cycle for Gaussian pulses [see Fig. 1(c)].

In principle, constructive interference between different quantum paths can only occur if the phase accumulated during distinct transition events is appropriately matched. Namely,

$$\Delta\phi_{ij}(\mathbf{k}) \approx \frac{\pi}{2}(1 - \mathrm{sgn}[\mathbf{E}(t_i)\mathbf{E}(t_j)]) + \frac{1}{\hbar}\int_{t_i}^{t_j} dt' \varepsilon_g(t'), \tag{3}$$

where $\mathrm{sgn}[\mathbf{E}(t_i)\mathbf{E}(t_j)]$ denotes the direction of electric field at two transition instants, t_i and t_j, respectively, while the second term corresponds to the dynamical phase [44,60]. For short trajectories, which contribute predominately, the influence of the first term can be disregarded, as it remains constant at π. Consequently, the nature of the interference, whether constructive or destructive, is primarily determined by the dynamical phase. This results in the formation of delocalized resonant rings under GP excitation (see the Supplemental Material [61] for details). However, a TP waveform, characterized by its asymmetric electric field, breaks the system's symmetry, causing a deviation of the localized CB distribution from the ring pattern.

To implement an intuitive physical picture, we further introduce a semiclassical trajectory analysis [30], to capture key aspects of the electron-hole dynamics in white-light IAP generation. As anticipated, the saddle-point solutions exhibit excellent agreement with time-frequency analysis (see Fig. S4 in the Supplemental Material [62]). This consistency enables an intuitive description of TP-driven electron-hole dynamics: (1) preacceleration at the valence band edge, (2) tunneling ionization-induced electron-hole pair generation in the vicinity of the band-gap minimum, followed by (3) propagating carrier motion in their respective bands. Since electrons at the Brillouin zone boundary display a dispersion that is opposite to those near the band-gap minima, the TP pulse manipulates the electron's position in k space, thereby reducing wave packet dispersion through its asymmetric temporal profile.

The robustness of the proposed strategy is subsequently evaluated by assessing the performance of diverse material systems in generating transform-limited broadband attosecond pulses (see the Supplemental Material S6 for details [63]). Using Landau-Zener-Stückelberg interferometry [64], the strong-field resonant excitation can be directly linked to the driving laser parameters via the following equation (see the Supplemental Material for details [65]):

$$\phi_{\mathrm{Stokes}} + \mathcal{D}(t) = n\pi, \tag{4}$$

where ϕ_{Stokes} is the Stokes phase accumulated in Landau-Zener transition. We demonstrate that the fulfillment of Eq. (4) depends primarily on dimensionless time ωt, electric field strength, and envelope shape, with negligible dependence on central frequency (see details in the Supplemental Material [65]). Therefore, an ideal envelope that satisfies Eq. (4) establishes an upper limit for the achievable pulse duration. For simplicity, we consider a cosine carrier with a central wavelength of 1.256 μm; the maximum achievable continuous bandwidth is shown in Fig. 4(a). The corresponding pulse duration limit based on the time-bandwidth limit of a Sech^2 waveform is shown in Fig. 4(b). The estimated pulse duration is in good agreement with our calculated results, indicating the robustness of the approach proposed here.

Having demonstrated the feasibility of generating white-light IAPs via waveform control, we now turn to its experimental implementation, a challenge hindered by the difficulty of shaping few-cycle laser pulses. This raises a natural question: Can white-light IAPs be generated using a multicycle field, which is more readily available in the laboratory? To address this, we emphasize the key idea of our approach: breaking the discrete time-translation symmetry

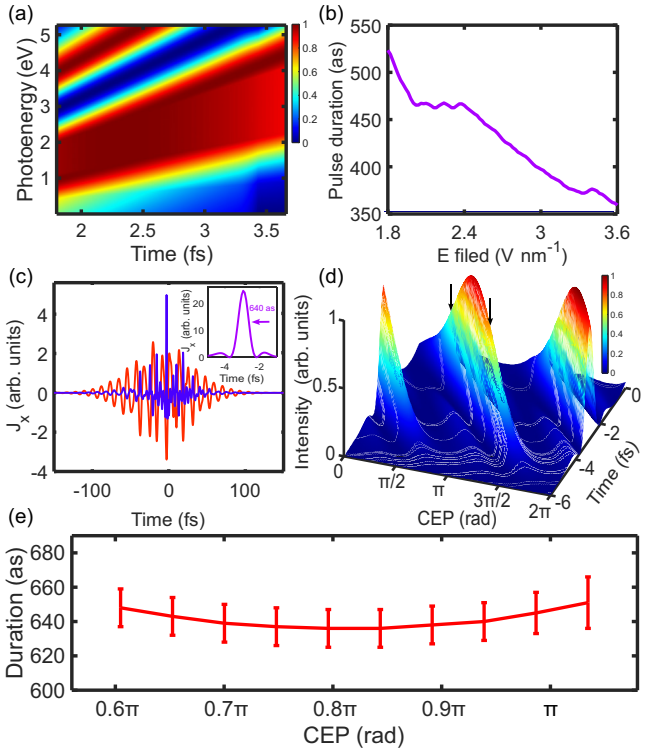

FIG. 4. (a) Dependence of the continuous spectrum in gapped graphene on peak field strength under ideal dispersion compensation condition. (b) The transform-limited pulse duration calculated based on panel (a), assuming a Sech^2 pulse shape (see the detailed laser parameters in the Supplemental Material [66]). (c) IAP generation driven by a multicycle laser field. The red and blue curves represent the driving laser field and generated isolated attosecond pulse, respectively. The inset shows the temporal profile of the IAP spectrum. (d) Yield of IAPs generated by the driving laser pulse in panel (c) across different CEP. (e) CEP-dependent pulse duration, derived from integration of the data between the arrows in panel (d).

of the driving field and the dynamical symmetries of the light-matter interaction to enable dispersion compensation via trajectory steering. Consistent with prior gas- and solid-HHG studies, the symmetry control in Fig. 2(a) is accomplished via CEP-stabilized few-cycle pulses and temporal gating. Alternatively, symmetry control can be ultimately achieved by engineering a Floquet time quasicrystal through the synthesis of a multicolor field with incommensurate frequency ratios, owing to its inherent quasiperiodicity. Building on this idea, we revisit our approach utilizing an experimentally accessible multicycle and multicolor field. The corresponding driving waveform and resulting harmonics are shown in Fig. 4(c) (detailed laser parameters can be found in the Supplemental Material [66]). Remarkably, an IAP pulse with its duration approximately equal to 640 as is obtained by applying our waveform optimization protocol to these multicycle and multicolor laser fields. On the other hand, CEP stabilization plays an essential role in generating IAPs from both gases and solids driven by few-cycle fields. To examine its influence on IAP generation by multicycle, multicolor fields, we analyze the Fourier-limited pulse duration under identical driving parameters while varying the CEP. The results are shown in Figs. 4(d) and 4(e). They demonstrate that the IAP intensity peaks at a CEP approximately equals to 0.8π, while the pulse duration remains constant as the CEP increases from 0.6π to 1.1π. Experimentally, the relative phase between the multicolor pulses can be stabilized and locked with a precision of less than 30 as [35,67]. Consequently, the considerably reduced necessity for CEP stability substantially weakens the experimental challenges associated with IAP generation.

In conclusion, by drawing an analogy to perturbative nonlinear optics and combining light-wave electron control techniques with strong-field resonant excitation dynamics, we have achieved the generation of linearly polarized and nearly circularly polarized IAPs in a wide range of material systems, demonstrating the versatility of this approach. Through systematic investigations of the underlying microscopic dynamics in both quantum and semiclassical pictures, we have demonstrated that tailoring the driving laser waveform enables intentional manipulation of electron-hole dynamics during light-matter interactions under strong-field excitation, resulting in a nearly continuous population distribution in momentum space. The present study bridges the critical gap in the generation of IAPs covering visible to ultraviolet wavelength range, which enables the steering of coherent electronic motions and brings new possibilities toward the realm of attochemistry [17,68,69] and related fields [55,56].

ACKNOWLEDGMENTS

This work was supported by the National Natural Science Foundation of China Grants No. 12474261 and No. 12450401 and the Synergic Extreme Condition User Facility (SECUF). H.T. acknowledges the support from National Key R&D Program of China (Grant No. 2022YFA1604200) and the National Natural Science Foundation of China (Grants No. 12034020 and No. 92250303).

DATA AVAILABILITY

No data were created or analyzed in this study.

[1] P. M. Paul, E. S. Toma, P. Breger, G. Mullot, F. Auge, P. Balcou, H. G. Muller, and P. Agostini, Observation of a train of attosecond pulses from high harmonic generation, Science **292**, 1689 (2001).

[2] M. Hentschel, R. Kienberger, C. Spielmann, G. A. Reider, N. Milosevic, T. Brabec, P. Corkum, U. Heinzmann, M. Drescher, and F. Krausz, Attosecond metrology, Nature (London) **414**, 509 (2001).

[3] M. Schultze, M. Fieß, N. Karpowicz, J. Gagnon, M. Korbman, M. Hofstetter, S. Neppl, A. L. Cavalieri, Y. Komninos, T. Mercouris, *et al.*, Delay in photoemission, Science **328**, 1658 (2010).

[4] K. Klünder, J. M. Dahlström, M. Gisselbrecht, T. Fordell, M. Swoboda, D. Guénot, P. Johnsson, J. Caillat, J. Mauritsson, A. Maquet, R. Taïeb, and A. L'Huillier, Probing single-photon ionization on the attosecond time scale, Phys. Rev. Lett. **106**, 143002 (2011).

[5] M. Isinger, R. J. Squibb, D. Busto, S. Zhong, A. Harth, D. Kroon, S. Nandi, C. L. Arnold, M. Miranda, J. M. Dahlström, E. Lindroth, R. Feifel, M. Gisselbrecht, and A. L'Huillier, Photoionization in the time and frequency domain, Science **358**, 893 (2017).

[6] G. Schmid, K. Schnorr, S. Augustin, S. Meister, H. Lindenblatt, F. Trost, Y. Liu, N. Stojanovic, A. Al-Shemmary, T. Golz, R. Treusch, M. Gensch, M. Kübel, L. Foucar, A. Rudenko, J. Ullrich, C. D. Schröter, T. Pfeifer, and R. Moshammer, Terahertz-field-induced time shifts in atomic photoemission, Phys. Rev. Lett. **122**, 073001 (2019).

[7] M. Huppert, I. Jordan, D. Baykusheva, A. von Conta, and H. J. Wörner, Attosecond delays in molecular photoionization, Phys. Rev. Lett. **117**, 093001 (2016).

[8] X. Gong, S. Heck, D. Jelovina, C. Perry, K. Zinchenko, R. Lucchese, and H. J. Wörner, Attosecond spectroscopy of size-resolved water clusters, Nature (London) **609**, 507 (2022).

[9] S. Heck, M. Han, D. Jelovina, J.-B. Ji, C. Perry, X. Gong, R. Lucchese, K. Ueda, and H. J. Wörner, Two-center interference in the photoionization delays of Kr_2, Phys. Rev. Lett. **129**, 133002 (2022).

[10] I. Jordan, M. Huppert, D. Rattenbacher, M. Peper, D. Jelovina, C. Perry, A. von Conta, A. Schild, and H. J. Wörner, Attosecond spectroscopy of liquid water, Science **369**, 974 (2020).

[11] S. Li, L. Lu, S. Bhattacharyya, C. Pearce, K. Li, E. T. Nienhuis, G. Doumy, R. D. Schaller, S. Moeller, M.-F. Lin, *et al.*, Attosecond-pump attosecond-probe x-ray spectroscopy of liquid water, Science **383**, 1118 (2024).

[12] A. L. Cavalieri, N. Müller, T. Uphues, V. S. Yakovlev, A. Baltuška, B. Horvath, B. Schmidt, L. Blümel, R. Holzwarth, S. Hendel, M. Drescher, U. Kleineberg, P. M. Echenique, R. Kienberger, F. Krausz, and U. Heinzmann, Attosecond spectroscopy in condensed matter, Nature (London) **449**, 1029 (2007).

[13] S. Neppl, R. Ernstorfer, E. M. Bothschafter, A. L. Cavalieri, D. Menzel, J. V. Barth, F. Krausz, R. Kienberger, and P. Feulner, Attosecond time-resolved photoemission from core and valence states of magnesium, Phys. Rev. Lett. **109**, 087401 (2012).

[14] M. Volkov, S. A. Sato, F. Schlaepfer, L. Kasmi, N. Hartmann, M. Lucchini, L. Gallmann, A. Rubio, and U. Keller, Attosecond screening dynamics mediated by electron localization in transition metals, Nat. Phys. **15**, 1145 (2019).

[15] F. Krausz and M. Ivanov, Attosecond physics, Rev. Mod. Phys. **81**, 163 (2009).

[16] A. L'Huillier, Nobel lecture: The route to attosecond pulses, Rev. Mod. Phys. **96**, 030503 (2024).

[17] F. Martín, F. Calegari, C. Vozzi, K. Ueda, and L. DiMauro, Virtual special issue on attosecond chemistry, J. Phys. Chem. A **128**, 4761 (2024).

[18] X. Feng, S. Gilbertson, H. Mashiko, H. Wang, S. D. Khan, M. Chini, Y. Wu, K. Zhao, and Z. Chang, Generation of isolated attosecond pulses with 20 to 28 femtosecond lasers, Phys. Rev. Lett. **103**, 183901 (2009).

[19] E. J. Takahashi, P. Lan, O. D. Mücke, Y. Nabekawa, and K. Midorikawa, Infrared two-color multicycle laser field synthesis for generating an intense attosecond pulse, Phys. Rev. Lett. **104**, 233901 (2010).

[20] M. Chini, K. Zhao, and Z. Chang, The generation, characterization and applications of broadband isolated attosecond pulses, Nat. Photon. **8**, 178 (2014).

[21] T. Gaumnitz, A. Jain, Y. Pertot, M. Huppert, I. Jordan, F. Ardana-Lamas, and H. J. Wörner, Streaking of 43-attosecond soft-X-ray pulses generated by a passively CEP-stable mid-infrared driver, Opt. Express **25**, 27506 (2017).

[22] J. Schötz, B. Förg, W. Schweinberger, I. Liontos, H. Masood, A. Kamal, C. Jakubeit, N. Kling, T. Paasch-Colberg, S. Biswas, M. Högner, I. Pupeza, M. Alharbi, A. Azzeer, and M. Kling, Phase-matching for generation of isolated attosecond XUV and soft-X-ray pulses with few-cycle drivers, Phys. Rev. X **10**, 041011 (2020).

[23] Y. Yang, R. E. Mainz, G. M. Rossi, F. Scheiba, M. A. Silva-Toledo, P. D. Keathley, G. Cirmi, and F. X. Kärtner, Strong-field coherent control of isolated attosecond pulse generation, Nat. Commun. **12**, 6641 (2021).

[24] M. Guan, S. Hu, H. Zhao, C. Lian, and S. Meng, Toward attosecond control of electron dynamics in two-dimensional materials, Appl. Phys. Lett. **116**, 043101 (2020).

[25] X.-Y. Wu, H. Liang, X.-S. Kong, Q. Gong, and L.-Y. Peng, Enhancement of high-order harmonic generation in two-dimensional materials by plasmonic fields, Phys. Rev. A **103**, 043117 (2021).

[26] Z. Nourbakhsh, N. Tancogne-Dejean, H. Merdji, and A. Rubio, High harmonics and isolated attosecond pulses from MgO, Phys. Rev. Appl. **15**, 014013 (2021).

[27] A. Sadeghifaraz, E. Irani, and M. Monfared, Efficient attosecond pulse generation from WS_2 semiconductor by tailoring the driving laser pulse, Opt. Commun. **516**, 128226 (2022).

[28] P. B. Corkum, Plasma perspective on strong field multiphoton ionization, Phys. Rev. Lett. **71**, 1994 (1993).

[29] S. Ghimire, A. D. DiChiara, E. Sistrunk, P. Agostini, L. F. DiMauro, and D. A. Reis, Observation of high-order harmonic generation in a bulk crystal, Nat. Phys. **7**, 138 (2011).

[30] G. Vampa, C. McDonald, G. Orlando, D. Klug, P. Corkum, and T. Brabec, Theoretical analysis of high-harmonic generation in solids, Phys. Rev. Lett. **113**, 073901 (2014).

[31] M. Wu, D. A. Browne, K. J. Schafer, and M. B. Gaarde, Multilevel perspective on high-order harmonic generation in solids, Phys. Rev. A **94**, 063403 (2016).

[32] M. Wu, S. Ghimire, D. A. Reis, K. J. Schafer, and M. B. Gaarde, High-harmonic generation from Bloch electrons in solids, Phys. Rev. A **91**, 043839 (2015).

[33] L. Li, P. Lan, X. Zhu, and P. Lu, High harmonic generation in solids: Particle and wave perspectives, Rep. Prog. Phys. **86**, 116401 (2023).

[34] See Supplemental Material S2 at http://link.aps.org/supplemental/10.1103/8x1z-3l7k for the description of connection between the dispperion of electron-hole wave packet and the chirp of coherent radiation, which includes Refs. [44,70].

[35] Z. Chen, M. Levit, Y. Kern, B. Roy, A. Goldner, and M. Krüger, Attosecond pulses from a solid driven by a synthesized two-

color field at megahertz repetition rate, ACS Photonics **12**, 2819 (2025).
[36] M. Shirozhan, S. Mondal, T. Grósz, B. Nagyillés, B. Farkas, A. Nayak, N. Ahmed, I. Dey, S. C. De Marco, K. Nelissen, *et al.*, High-repetition-rate attosecond extreme ultraviolet beamlines at ELI ALPS for studying ultrafast phenomena, Ultrafast Sci. **4**, 0067 (2024).
[37] A. Nayak, D. Rajak, B. Farkas, C. Granados, P. Stammer, J. Rivera-Dean, T. Lamprou, K. Varju, Y. Mairesse, M. F. Ciappina, *et al.*, Attosecond metrology of vacuum-ultraviolet high-order harmonics generated in semiconductors via laser-dressed photoionization of alkali metals, Nat. Commun. **16**, 1428 (2025).
[38] S. Ghimire and D. A. Reis, High-harmonic generation from solids, Nat. Phys. **15**, 10 (2019).
[39] Á. Jiménez-Galán, R. E. Silva, O. Smirnova, and M. Ivanov, Sub-cycle valleytronics: Control of valley polarization using few-cycle linearly polarized pulses, Optica **8**, 277 (2021).
[40] Y.-L. He, J. Guo, F.-Y. Gao, Z.-J. Yang, S.-Q. Zhang, and X.-S. Liu, Interference between harmonics of different crystal momentum channels in solid high-order harmonic generation, Phys. Rev. A **104**, 013104 (2021).
[41] See Supplemental Material S13 at http://link.aps.org/supplemental/10.1103/8x1z-3l7k for details on the dynamical evolution of the residual CB population and phase.
[42] T. Higuchi, C. Heide, K. Ullmann, H. B. Weber, and P. Hommelhoff, Light-field-driven currents in graphene, Nature (London) **550**, 224 (2017).
[43] M. Du, C. Liu, Y. Zheng, Z. Zeng, and R. Li, Attosecond transient-absorption spectroscopy in one-dimensional periodic crystals, Phys. Rev. A **100**, 043840 (2019).
[44] S. A. Oliaei Motlagh, J.-S. Wu, V. Apalkov, and M. I. Stockman, Femtosecond valley polarization and topological resonances in transition metal dichalcogenides, Phys. Rev. B **98**, 081406(R) (2018).
[45] See Supplemental Material S9 at http://link.aps.org/supplemental/10.1103/8x1z-3l7k for discussion on the effect of Berry curvature in white-light IAP generation.
[46] A. Bharti, M. Mrudul, and G. Dixit, High-harmonic spectroscopy of light-driven nonlinear anisotropic anomalous Hall effect in a Weyl semimetal, Phys. Rev. B **105**, 155140 (2022).
[47] L. Zheng, S. Tang, and X. Chen, Isolated sub-100-as pulse generation by optimizing two-color laser fields using simulated annealing algorithm, Opt. Express **17**, 538 (2009).
[48] Y. He, L. He, P. Lan, B. Wang, L. Li, X. Zhu, W. Cao, and P. Lu, Direct imaging of molecular rotation with high-order-harmonic generation, Phys. Rev. A **99**, 053419 (2019).
[49] See Supplemental Material S11 at http://link.aps.org/supplemental/10.1103/8x1z-3l7k for the description of simulated annealing.
[50] M. Mrudul, Á. Jiménez-Galán, M. Ivanov, and G. Dixit, Light-induced valleytronics in pristine graphene, Optica **8**, 422 (2021).
[51] See Supplemental Material S4 at http://link.aps.org/supplemental/10.1103/8x1z-3l7k for details on derivations of interband current, which includes Refs. [71,72].
[52] See Supplemental Material S10 at http://link.aps.org/supplemental/10.1103/8x1z-3l7k for discussion on the effect of dephasing time.
[53] N. Rana, M. Mrudul, and G. Dixit, Generation of circularly polarized high harmonics with identical helicity in two-dimensional materials, Phys. Rev. Appl. **18**, 064049 (2022).
[54] R. Rajpoot, A. R. Holkundkar, N. Rana, and G. Dixit, Tailoring polarisation of attosecond pulses via co-rotating bicircular laser fields, Phys. Lett. A **493**, 129241 (2024).
[55] M. Fanciulli, H. Volfová, S. Muff, J. Braun, H. Ebert, J. Minár, U. Heinzmann, and J. H. Dil, Spin polarization and attosecond time delay in photoemission from spin degenerate states of solids, Phys. Rev. Lett. **118**, 067402 (2017).
[56] D. Bauer and K. K. Hansen, High-harmonic generation in solids with and without topological edge states, Phys. Rev. Lett. **120**, 177401 (2018).
[57] See Supplemental Material Table S1 at http://link.aps.org/supplemental/10.1103/8x1z-3l7k for the detailed laser parameters used to generate white-light IAP.
[58] O. Melchert, B. Roth, U. Morgner, and A. Demircan, OptFROG—Analytic signal spectrograms with optimized time–frequency resolution, SoftwareX **10**, 100275 (2019).
[59] K. Uchida, S. Kusaba, K. Nagai, T. N. Ikeda, and K. Tanaka, Diabatic and adiabatic transitions between Floquet states imprinted in coherent exciton emission in monolayer WSe_2, Sci. Adv. **8**, eabq7281 (2022).
[60] M. S. Wismer, S. Y. Kruchinin, M. Ciappina, M. I. Stockman, and V. S. Yakovlev, Strong-field resonant dynamics in semiconductors, Phys. Rev. Lett. **116**, 197401 (2016).
[61] See Supplemental Material S12 at http://link.aps.org/supplemental/10.1103/8x1z-3l7k for dicussion on the multiphoton excitation pattern under GP and TP excitation conditions.
[62] See Supplemental Material S8 at http://link.aps.org/supplemental/10.1103/8x1z-3l7k for details on derivation about saddle-point method and results.
[63] See Supplemental Material S6 at http://link.aps.org/supplemental/10.1103/8x1z-3l7k for detailed description of IAP temporal profile generated from different materials and corresponding driven laser parameters and materials' model.
[64] O. Ivakhnenko, S. Shevchenko, and F. Nori, Quantum control via Landau–Zener–Stückelberg–Majorana transitions, Phys. Rep. **995**, 1 (2023).
[65] See Supplemental Material S14 at http://link.aps.org/supplemental/10.1103/8x1z-3l7k for details on derivation and plots for strong field resonance parameter and their relation with driving pulse parameters, which includes Ref. [73].
[66] See Supplemental Material Table S5 at http://link.aps.org/supplemental/10.1103/8x1z-3l7k for details on long-pulse duration driven pulse parameter.
[67] C. Manzoni, O. D. Mücke, G. Cirmi, S. Fang, J. Moses, S.-W. Huang, K.-H. Hong, G. Cerullo, and F. X. Kärtner, Coherent pulse synthesis: Towards sub-cycle optical waveforms, Laser Photonics Rev. **9**, 129 (2015).
[68] H. J. Wörner, C. A. Arrell, N. Banerji, A. Cannizzo, M. Chergui, A. K. Das, P. Hamm, U. Keller, P. M. Kraus, E. Liberatore, *et al.*, Charge migration and charge transfer in molecular systems, Struct. Dyn. **4**, 061508 (2017).

[69] I. C. D. Merritt, D. Jacquemin, and M. Vacher, Attochemistry: Is controlling electrons the future of photochemistry? J. Phys. Chem. Lett. **12**, 8404 (2021).

[70] W. Houston, Acceleration of electrons in a crystal lattice, Phys. Rev. **57**, 184 (1940).

[71] C. Liu, Y. Zheng, Z. Zeng, and R. Li, Driving-laser ellipticity dependence of high-order harmonic generation in graphene, Phys. Rev. A **97**, 063412 (2018).

[72] D. Dimitrovski, T. G. Pedersen, and L. B. Madsen, Floquet-Bloch shifts in two-band semiconductors interacting with light, Phys. Rev. A **95**, 063420 (2017).

[73] C. Heide, T. Boolakee, T. Higuchi, and P. Hommelhoff, Adiabaticity parameters for the categorization of light-matter interaction: From weak to strong driving, Phys. Rev. A **104**, 023103 (2021).